Effects of q-profile structures on intrinsic torque reversals

Z. X. Lu[1,2], W. X. Wang[3], P. H. Diamond[2], G. Tynan[1,2], S. Ethier[3], J. Chen[3], C. Gao[4] and J. E. Rice[4]

[1] Center for Energy Research and Department of Mechanical and Aerospace Engineering, University of California at San Diego, San Diego, California, USA
[2] Center for Momentum Transport and Flow Organization and Center for Astrophysics and Space Science, University of California, San Diego, CA 92093-0424, USA
[3] Princeton Plasma Physics Laboratory, Princeton, NJ 08540, USA
[4] Plasma Science and Fusion Center, Massachusetts Institute of Technology, Cambridge, MA 02139, USA

Abstract. Changes in rotation have been observed in LHCD experiments. From these observations, reversals in intrinsic torque have been inferred. This paper identifies the mechanism for intrinsic torque reversal linked to magnetic shear ($\hat{s}$). Gyrokinetic simulations demonstrate that as compared to the normal $\hat{s}$ case, the intrinsic torque reverses, for $\hat{s} < \hat{s}_{crit}$. Analysis shows that the reversal occurs due to the dominance of the symmetry breaking mechanism in residual stress due to the synergy of toroidal coupling and the intensity gradient. This mechanism is a consequence of ballooning structure at weak $\hat{s}$. Gyrokinetic simulation gives $\hat{s}_{crit} \approx 0.3$ for trapped electron modes (TEM) and $\hat{s}_{crit} \approx 1.1$ for ion temperature gradient (ITG) modes. The value of $\hat{s}_{crit}$ is consistent with results from the Alcator C-Mod LHCD experiments, for which $\hat{s} > 0$ in the whole plasma column and $\hat{s}^{exp}_{crit} \approx 0.2 \sim 0.3$ [J. Rice et al, Phys. Rev. Lett. 111, 125003].

Keywords: momentum transport, intrinsic rotation, gyrokinetic turbulence

1. Introduction

The origin of intrinsic or spontaneous flows is a key issue for the understanding of various physics phenomena, e.g., solar differential rotation [1], formation of the tachocline [2] and atmospheric jet stream [3], etc. In tokamak plasmas, toroidal rotation can develop due to intrinsic torque density τ_I, i.e., the divergence of residual stress $\mathbf{\Pi}^R_{r\phi}$, without direct external momentum injection [4, 5]. As an efficient mechanism to mitigate macroscopic instability [6] and regulate turbulent transport, intrinsic rotation is particularly important for International Thermonuclear Experimental Reactor (ITER), since neutral beam injection (NBI) is not sufficient to drive the requisite rotation on large tokamaks.

Rotation reversal experiments on tokamak devices—both Ohmic ones [7] and otherwise[8, 9]—present a compelling challenge to our understanding of intrinsic torque and might have connections to dynamo reversal phenomena. In recent studies of rotation with lower hybrid current drive (LHCD) on Alcator C-Mod, ΔV_ϕ reversed from high P_{LH} (lower hybrid wave power) to low P_{LH} discharges, where ΔV_ϕ is the change of toroidal velocity in the core ($r/a < 0.5$) during LHCD [9]. In these discharges, high P_{LH} corresponds to high plasma current I_p, low q and normal (or relatively high) core $\hat{s}$ (magnetic shear), and vice versa for low P_{LH}. Motivated by experimental evidence [9, 10] and theoretical understanding [5], it is hypothesized that ΔV_ϕ is due to the reversal in the underlying intrinsic torque. In the plasma core, the toroidal torque during LHCD is in the counter-current direction when $\hat{s}$ is normal and reverses when $\hat{s}$ is lower than a critical value $\hat{s}_{crit}$. In these discharges, $\hat{s}$ is always above zero, increases monotonically with r, and rotation changes mainly for $r/a < 0.5$. Thus $\hat{s}_{crit}$ is estimated at $r/a \sim 0.3$. Experimental results indicate that torque reversal occurs for $\hat{s} < \hat{s}^{exp}_{crit} \approx 0.2 \sim 0.3$. Understanding the effect of the q-profile on intrinsic torque is also an issue of interest in the context of internal transport barrier (ITB) formation and profile "de-stiffening", which occur in both reversed and weakly positive magnetic shear [11].

The recent theoretical development, simulation studies and experimental observations provide understanding of the intrinsic rotation (see [5, 12] and references therein). The suggested mechanism for residual stress generation includes, but is not limited to, radial profile shearing effects [13], up-down asymmetry of the equilibrium [14], shear flow induced by mean E_r [15] or zonal E_r [16], and turbulent acceleration [17, 18]. To the lowest order in the normalized Larmor radius ρ_*, the poloidal tilt of the global mode structure arising from the "profile shearing" (the radial variation of the equilibrium profiles) leads to a finite residual stress as demonstrated in [13]. On the other hand, based on the fluid model and the sheared slab geometry, it has been suggested that the turbulence intensity gradient can lead to finite parallel wave vector $\langle k_\parallel \rangle$ and thus to finite residual stress [19]. Heuristically, by combining the intensity gradient mechanism and the mode structure "tilt" theory, the residual stress can be written as

$$\Pi_{r\phi} = \alpha \hat{s} \frac{\partial I}{\partial r} + \Pi^{tilt}_{r\phi}(\hat{\theta}^R_k, T, n \ldots) \quad , \tag{1}$$

where I is the turbulence intensity, α is a function of other variables (see Eq. (3) of [19] for a model equation), $\Pi_{r\phi}^{tilt}$ is the residual stress related to the profile shearing induced mode structure "tilt" [13], and "R" in $\hat{\theta}_k^R$ means that the "tilting" angle is a real number. Although recent gyrokinetic simulations demonstrated the dominance of the profile shearing effect related to "tilting" angle over the turbulence intensity effect on the residual stress generation [20], the study therein is limited to a specific parametric regime ($\hat{s}$, mode type, etc). In broader parametric regimes, the dominance of either mode structure "tilt" or turbulence gradient effects is inconclusive. Meanwhile, some basic issues remain to be clarified. First, the effect of the q profile, especially the magnetic shear, on intrinsic torque remains unclear although recent experimental observations demonstrated its possible effect on intrinsic torque reversal [9]. In addition, the residual stress and intrinsic rotation generation at weak magnetic shear regime are of particular interest because of their potential impact on ITB formation, which occurs not only in negative magnetic shear but also in regimes of weakly positive magnetic shear [11]. Second, the local (in r direction) simulation of the residual stress [13] takes a real number $\hat{\theta}_k^R$, the "tilting angle", as the input parameters but the effect of the turbulence intensity radial gradient on parallel mode structure has not been considered on the same footing and the corresponding studies rely on global simulations. As a result, a framework needs to be developed to describe both the "tilting" mode structure mechanism and the turbulence intensity mechanism in terms of a theoretical tractable form. Last, although the ITG-TEM transition has been suggested as the intrinsic torque reversal mechanism, its applicability regime needs to be verified. As to be shown in Table 2, the ITG-TEM transition induced intrinsic torque reversal due to intensity gradient only occurs in a specific magnetic shear regime.

In this work, we report new features of the symmetry breaking of the parallel wave vector and the residual stress, which emerge as dominant at low $\hat{s}$ and leads to intrinsic torque reversal. The underlying mechanism is due to the synergy of toroidal coupling and intensity gradient, which leads to significant radial eigenfunction shift and residual stress orientation change at weak $\hat{s}$. Heuristically, Eq. (1) can be rewritten as

$$\Pi_{r\phi} = \alpha(\hat{s} - \hat{s}_{crit})\frac{\partial I}{\partial r} + \Pi_{r\phi}^{tilt}(\hat{\theta}_k^R, T, n \ldots) \quad , \tag{2}$$

where $\hat{s}_{crit}$ is around 0.3 for TEM and 1.1 for ITG according to our simulation of a model case in section 2. The value of $\hat{s}_{crit}$ changes slightly for Alcator C-Mod plasmas as shown in section 5. The critical value of $\hat{s}_{crit}$ is set by the competition between magnetic drift and ion finite Larmor radius (FLR) effects. Most previous works on residual stress focused on normal $\hat{s}$ regimes [19, 21], so the mechanism proposed in this paper complements to previously proposed mechanisms [13, 19]. Based on our simulations and analyses, the calculated intrinsic torque direction and the critical magnetic shear for torque reversal are consistent with experimental observations on Alcator C-Mod. The novelty of this work can be demonstrated by drawing its connection to the profile shearing effect [13] and the intensity gradient mechanism [19] using the complex mixed WKB-full-wave approach for the 2D mode structure analysis [22], as shown in table 1.

"Profile shearing" refers to the "radial variation of the equilibrium" which leads to the "poloidal tilt of the global mode structure" in [13]. More generally, the radial variation (e.g., first and second derivative of the profiles) can leads to both the radial propagation and radial envelope variation of the mode, as shown later. The consequent symmetry breaking of the mode structure occurs not only in the configuration space (up-down symmetry breaking of mode structure in θ direction), but also in spectrum space ($k_{\|}$ symmetry breaking). As a result, the "radial variation" in this work has more general meaning than the "profile shearing" in [13]. The intrinsic torque reversal found in our study is connected to the radial mode shift away from its rational mode surface (RMS) at weak magnetic shear and thus is not the mechanism introduced in [19], which is based on sheared magnetic field slab geometry where the radial mode shift is assumed to be zero. This reversal is also not captured in [13] since the reversal observed in our work is not merely due the radial propagation and since the "tilting" angle does not change orientation as the intrinsic torque reverses. Although this mechanism is already included in a properly implemented global gyrokinetic code, identifying this mechanism requires the understanding of the generalized symmetry breaking mechanism due to the radial variation with both mode structure tilt and intensity (or envelope amplitude) gradient included.

Table 1. The generalized symmetry breaking mechanism due to the radial variation using the complex mixed WKB-full-wave approach (mixed approach) [22] and its connection to the profile shearing mechanism [13] and turbulence intensity gradient mechanism [19].

Symmetry breaking source	Symmetry breaking of the mode structure	Phenomenon and related work	Variables used in the mixed approach
Radial variation	up-down symmetry breaking (configuration space)	global mode structure "tilt", or poloidal shift of turbulence maximum [13]	$\hat{\theta}_k^R \equiv Re\{\frac{-i}{nq'}\frac{d}{dr}\ln A\}$
	$k_{\|}$ symmetry breaking (spectrum space)	turbulence intensity gradient [19], or radial envelope variation	$\hat{\theta}_k^I \equiv Im\{\frac{-i}{nq'}\frac{d}{dr}\ln A\}$, A is the radial envelope

2. Global gyrokinetic simulations using GTS

2.1. GTS code and simulation parameters

We use the GTS code [16, 23] and consider typical tokamak parameters [24]. GTS is a global gyrokinetic, particle-in-cell, δf code. With the capability of capturing the global effects such as the turbulence intensity gradient and propagation in the radial direction from the normal to weak $\hat{s}$ regime in realistic three dimensional (3D) geometry, GTS is well suited for the study of q profile effects in this work. The equilibria used in our study are generated using the Equilibrium and Stability Code (ESC) [25], with q and

pressure profiles specified. The model equilibria in this section are characterized by on-axis magnetic field value $B_{axis} \approx 2$, major radius $R_0 = 2.5$, minor radius $a = 0.7$, outer boundary elongation $E = 1.45$, and triangularity $\kappa = 0.144$. Shown in Fig. 1 are the q profiles with on-axis q_{min} and off-axis q_{min} for qualitative studies in Figs. 2, 5, 6. The off-axis q_{min} profiles are represented by the normal (positive) $\hat{s}$ and weakly positive $\hat{s}$ cases. For quantitative parametric scans in Figs. 3, 4, 7, 12, the q profile with on-axis q_{min} is specified as

$$q = q_0 \exp\{C_0 r^{C_1}\} \ , \tag{3}$$

where the radial-like coordinate $r = \sqrt{\Psi_t/\Psi_{t,edge}}$ is the square root of the normalized toroidal magnetic flux. The values of q_0, C_0 and C_1 are determined by three input variables q_e, q_c and $\hat{s}_c$, which are the safety factor at the edge and the reference radius r_c, and the magnetic shear at r_c. Profiles of temperature and density gradient are given by

$$\frac{R_0}{L_X} = \kappa_X \exp\left\{-\left(\frac{r - r_c}{r_{w,X}}\right)^2\right\} \tag{4}$$

where the subscript X indicates T_i, Te and n_e ($n_e = n_i$ has been assumed). The value of r_w is related to the curvature (or the second derivative) of the temperature and density profiles. If $r_w = 0.325$ is chosen, the R_0/L_X profile is close to the profiles used in other works [13, 20]. However, the value $r_w = 0.2$ used in this section is more relevant to the base case we defined for the C-Mod LHCD rotation experiment as to be demonstrated in section 5. The temperature and density profiles are chosen according to their gradient profiles and their values at the reference radius r_c, $T_i = T_e = 3.5keV$, $n_i = n_e = 1.6\times10^{13}/cm^3$. Here $a/\rho_i(r = r_c) \approx 160$, where $\rho_i = \upsilon_{ti}/\Omega_i$ and $\upsilon_{ti} \equiv \sqrt{T_i/m_i}$. The turbulence develops around r_c, where $\hat{s}(r_c)$ and $q(r_c)$ have a specific values; thus the effects of $\hat{s}$ and q on $\Pi^R_{r\phi}$ can be studied by changing $\hat{s}(r_c)$ and $q(r_c)$. In GTS, Coulomb collisions between like particles are implemented via a linearized Fokker-Plank operator with particle, momentum and energy conservation while electron-ion collisions are simulated by the Lorentz operator [26]. In our simulations, collisions are included for self-consistency. In GTS, it is optional to include the equilibrium radial electric field (E_{r0}) which can be calculated according to the radial force balance equation consistent with the toroidal rotation profile [27] or by a global neoclassical code GTC-Neo [28]. However, we will show that the symmetry breaking due to $\mathbf{E_{r0}} \times \mathbf{B}$ flow shear is not the dominant effect of intrinsic torque reversal from normal to weakly positive $\hat{s}$ in section 3 according to the comparison of simulations with and without the $\mathbf{E}_{r0} \times \mathbf{B}$ flow. The neoclassical effect in GTS can be included by retaining the relevant terms in the gyro-kinetic equation while using the initially loaded shifted Maxwellian distribution function [29]. However, in this work, we focus on global physics effects associated with finite ρ^* and profile/turbulence-intensity variations while the neoclassical effect on momentum transport [30, 31] is not considered. More detailed description of the gyro-kinetic simulation model implemented in GTS code can be found in [29].

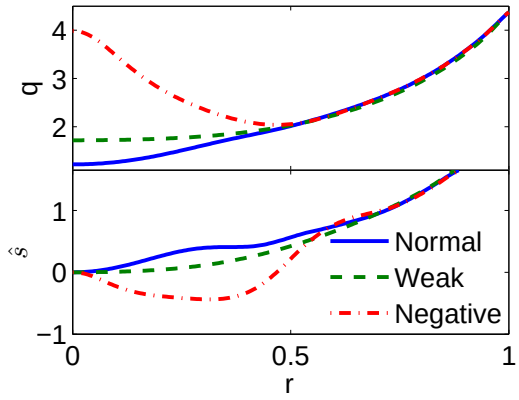

Figure 1. The q profiles with normal (positive) magnetic shear, weakly positive shear and negative magnetic shear.

The simulation is performed using the electro-static GTS version with fully kinetic electrons and real mass ratio $m_i/m_e = 3672$ for deuterium plasmas. The simulation grid spacing in radial and poloidal directions is the local Larmor radius ρ_i. For simulations in this section, we choose $N_r = 70 \sim 110$ in the radial direction, $N_\phi = 32$ in the toroidal direction in simulation domain with $0.1 < r < 0.8$ (nonlinear simulation) or $0.2 < r < 0.8$ (linear simulation). Due to the field-line following grid, the number of toroidal modes allowed in the system is not limited by N_ϕ. For the purpose of this work, the nonlinear simulations are performed on the turbulence time scale, around $400 \sim 600\ L_T/v_{ti}$ and with 40 particles per cell. As a result, the noise over signal ratio can be readily controlled at a low level compared to simulations on a much longer transport time scale [32]. On this time scale the turbulence gets saturated and the spectrum reaches approximately steady state. The toroidal momentum flux is calculated as

$$\Pi_{r\phi} = \left\langle \int d^3v m_i R v_\phi v_E \cdot \nabla r / |\nabla r| \delta f_i \right\rangle \quad , \tag{5}$$

where $\langle \ldots \rangle$ indicates the flux surface average, v_E is the $\mathbf{E} \times \mathbf{B}$ drift and v_ϕ is the full velocity in toroidal direction including the toroidal projection of the parallel and perpendicular velocities. For nonlinear simulations, the average of $\Pi_{r\phi}$ is obtained during several decorrelation time cycles (approximated by the inverse drift wave linear growth rate [33]) so that the statistical error is thought to be well below the signal.

2.2. Intrinsic torque reversal for weakly positive and negative $\hat{s}$ compared to that for normal $\hat{s}$

We first study the intrinsic torque reversal with reversed $\hat{s}$ and compare to that for normal $\hat{s}$. Here "normal $\hat{s}$" refers to a base case with on-axis q_{min} profile and $\hat{s}(r_c = 0.5) \approx 0.6$ at the reference radius r_c, while "reversed $\hat{s}$" refers to the case with an off-axis q_{min} profile and $\hat{s}(r_c = 0.4) \approx -0.3$ as shown in Fig. 1. The value of the

reference radius is set to $r_c = 0.5$ and 0.4 respectively so that even after the turbulence spreads in the radial direction, the overall effect of $\hat{s}(r_c)$ is evident. We choose $\kappa_{Ti} = 0$ to eliminate the ion temperature gradient (ITG) instability and focus on trapped electron mode (TEM) turbulence. The ITG case is discussed later. We choose $\eta_e \equiv \kappa_{Te}/\kappa_{ne} = 2$, $\kappa_{ne} = 2.25$ for normal shear and $\kappa_{ne} = 3$ for reversed shear to compensate the stabilizing effects of the reversed $\hat{s}$. The radial profiles of the residual stress are shown in Fig. 2. In the linear and nonlinear simulations, all the toroidal modes are kept without applying a spectrum filter and thus the residual stress for linear cases is mainly contributed by the most unstable mode. For the nonlinear simulation, the toroidal mode spectrum has a down shift (see Fig. 9 of [34] for the picture of spectrum down shift during nonlinear stage). Compared with the normal $\hat{s}$ case (Fig. 2 A), the orientation of the residual stress for the reversed $\hat{s}$ case changes, as shown in Fig. 2 B. Since the divergence of residual stress gives the intrinsic torque, i.e., $\tau_I = -\nabla\cdot\mathbf{\Pi}^R_{r\phi}$, the orientation change of the $\Pi^R_{r\phi}$ radial profile indicates intrinsic torque reversal. By comparing the radial structure of $\Pi^R_{r\phi}$ in the linear (blue lines) and nonlinear (black circles) stage, we found that the radial profile of $\Pi^R_{r\phi}$ maintains a similar structure. A parametric scan is performed in reversed $\hat{s}$ regime with $\hat{s}(r_c)$ ranging from -0.4 to 0. The intrinsic torque reversal is found if $\hat{s}(r_c) < 0$, demonstrating reversed $\hat{s}$ as a sufficient condition for intrinsic torque reversal. One key question is whether a reversed $\hat{s}$ is also necessary for intrinsic torque reversal or whether a weakly positive $\hat{s}$ is sufficient.

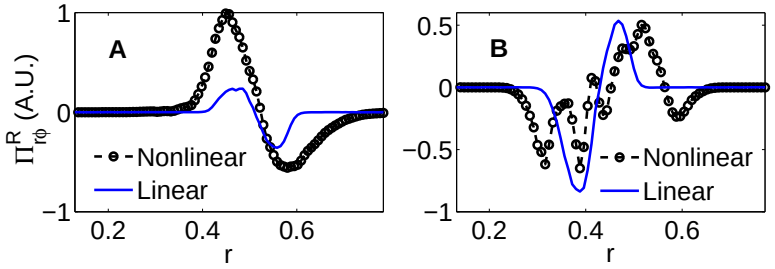

Figure 2. Radial profiles of residual stress in linear (blue lines) and nonlinear (black circles) stages for normal (A) and reversed (B) magnetic shear with $\hat{s}(r_c) \sim 0.6, -0.3$ respectively.

To determine the condition for reversal, we examine the radial structure of $\Pi^R_{r\phi}$ at weakly positive $\hat{s}$ and identify the critical magnetic shear value $\hat{s}_{crit}$ at which the intrinsic torque reverses. Different q profiles are generated based on Eq. (3) with different $\hat{s}$ values but fixed q at $r_c = 0.5$, as shown in Fig. 3 A and B. The other parameters are the same as those in the previous reversed magnetic shear case. The orientation of residual stress is found to reverse when $\hat{s}(r_c)$ decreases from 0.4 to 0.2, as shown in Fig. 3 D and E. More parametric scans indicate that the transition of residual stress orientation occurs at $\hat{s} \approx 0.3$. This result shows that the intrinsic torque can thus reverse if $\hat{s}$ is lower than a critical, positive value $\hat{s}_{crit}$ but not vanishing $\hat{s}$ as indicated by previous intensity gradient mechanism [19]. It has been shown that the shear reversal is not required. Another set of parametric scans is performed with fixed $\hat{s}$ profile but varying q values

at $r_c = 0.5$, i.e., $\hat{s}(r_c) = 0.4$ and $q(r_c)$ varying from 0.94 to 2.06. It is found that the residual stress profiles have the same orientation although q changes significantly. Thus the change in $\hat{s}$ leads to intrinsic torque reversal while change in q has no significant effect. This observation helps understand the torque reversal in the Alcator C-Mod LHCD experiment for weak $\hat{s}$ [9].

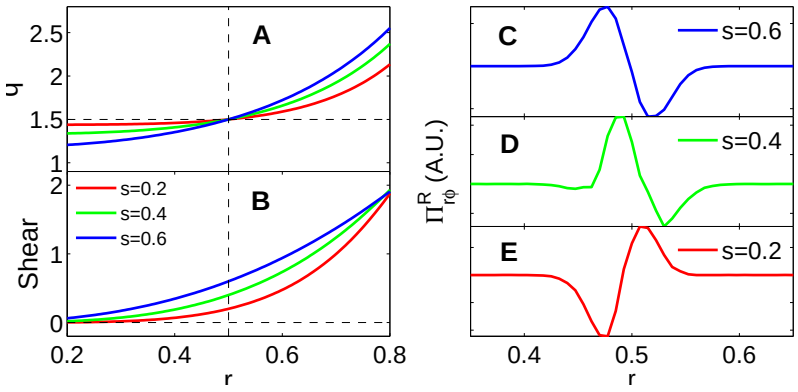

Figure 3. q and $\hat{s}$ profiles (left); residual stress profiles (right). Residual stress profile changes its orientation for $\hat{s}(r_c) = 0.2$ (E) compared to that with $\hat{s}(r_c) = 0.6$ (C), 0.4 (D).

In addition to TEM turbulence, ITG turbulence is also studied. We choose $\kappa_{Ti} = 4.5$, $\kappa_{Te} = 1.125$ and $\kappa_n = 1.5$ for the parametric scan using GTS. The critical magnetic shear for ITG-driven intrinsic torque reversal is found to be $\hat{s}^{ITG}_{crit} \approx 1.1$. The direction of the intrinsic torque, based on the divergence of residual stress at the small minor radius side of the intensity peak, is summarized in Table 2. It is shown that the intrinsic torque reverses from $\hat{s} > \hat{s}^{ITG}_R$ to $\hat{s} < \hat{s}^{TEM}_{crit}$, both for ITG and TEM turbulence. In addition, an intermediate shear region exists, where intrinsic torque for ITG and TEM turbulence has opposite directions. As a result, it is important to know the magnetic shear regime and the mode type in predicting the direction of intrinsic torque. The question of intrinsic torque in mixed states merits attention. Note that the accurate value of $\hat{s}_{scrit}$ might also be influenced by other parameters (T_i and T_e gradient, curvature etc) and thus can be different than $\hat{s}^{TEM}_{crit} \approx 0.3$ and $\hat{s}^{ITG}_{crit} \approx 1.1$ for different tokamak plasmas.

Table 2. Summary of the torque direction of ITG/TEM at the small minor radius side of the intensity peak. $\hat{s}^{TEM}_{crit} \approx 0.3$, $\hat{s}^{ITG}_{crit} \approx 1.1$.

	$\hat{s} > \hat{s}^{ITG}_R$	$\hat{s}^{TEM}_{crit} < \hat{s} < \hat{s}^{ITG}_{crit}$	$\hat{s} < \hat{s}^{TEM}_{crit}$
TEM	I. counter	II. *counter*	III. co
ITG	IV. counter	V. *co*	VI. co

Besides the orientation of the residual stress, the normalized residual stress is

calculated according to [13]

$$\bar{\Pi}_{r\phi} \equiv \frac{\Pi_{r\phi}}{Q_i}\frac{v_{ti}}{R_0} \quad , \quad Q_i \equiv \left\langle \int d^3v \frac{1}{2} m_i v^2 v_E \cdot \nabla r / |\nabla r| \delta f_i \right\rangle \quad . \tag{6}$$

Since the wave intensity vanishes outside of $0.4 < r < 0.6$ as shown in Fig. 3, we only show the normalized residual stress $\hat{\Pi}_{r\phi}$ in this region. Figure 4 demonstrates the radial structure of $\hat{\Pi}_{r\phi}$ with different $\hat{s}(r_c)$. We choose the ITG case ($\kappa_{Ti} = 4.5$, $\kappa_{Te} = 1.125$, $\kappa_n = 1.5$) for the comparison with the previous work [20]. The parametric scan is performed with $\hat{s}(r_c) = 0.6$, 0.8, 1.0 and 1.25. The most unstable mode has the poloidal mode number $m = 41$, 32, 31, 31. The corresponding poloidal wave vector is calculated according to $k_\theta = m/\langle r \rangle$ where $\langle r \rangle$ is estimated on the flux surface, which yields $k_\theta \rho_i = 0.48, 0.38, 0.37, 0.37$ respectively. For $\hat{s} = 1.0$, $\hat{\Pi}_{r\phi}$ is negative in the whole range, with a value around -0.04 (the average value is -0.0374 for $0.4 < r < 0.6$), which is close to $\Pi_{r\phi} v_{ti}/(Q_i R_0) \approx -0.06/(1.3 \times \sqrt{2}) \approx -0.03$ in Fig. 6 of [20] ($\sqrt{2}$ is due to the different definition of v_{ti}). This radial structure of $\hat{\Pi}_{r\phi}$ for $\hat{s} = 1.0$ is also reminiscent of Fig. 3 of [20], where the simulation was performed at $\hat{s}(r_c) = 0.78$ and $\Pi_{r\phi}$ was negative over the entire radial domain. However, as $\hat{s}(r_c)$ deviates from 1, the dipole structure of $\Pi_{r\phi}$ appears and it supports the turbulence intensity gradient mechanism for residual stress generation. It should be noted that the global mode tilt at various $\hat{s}(r_c)$ has the same direction for all cases in Fig. 4, and that thus the orientation change of the residual stress is not due to the tilting angle reversal, which is relevant to ITG-TEM transition [13].

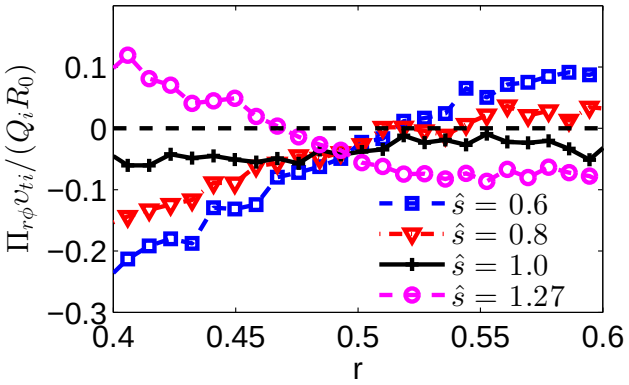

Figure 4. The normalized residual stress versus r for different values of magnetic shear $\hat{s}(r = r_c)$.

3. The identification of the intrinsic torque reversal mechanism based on correlation and sensitivity studies

Correlation and sensitivity studies are performed to identify the origin of the residual stress. We focus on the weakly positive magnetic shear case with $\hat{s}(r_c = 0.3) \approx 0.1$ as

shown in Fig. 1 (green dashed line). The correlation coefficient is calculated as follows

$$C[A,B] = \frac{\sum_i \left[A(r_i) - \bar{A}\right]\left[B(r_i) - \bar{B}\right]}{\sqrt{\sum_i \left[A(r_i) - \bar{A}\right]^2 \sum_i \left[B(r_i) - \bar{B}\right]^2}} \ , \tag{7}$$

which describes the similarity of two sets of radial profiles at a given time and where $\bar{A}$ and $\bar{B}$ are the average values along r, and the summations are performed in the radial domain. The coefficient describes the similarity between two radial profiles. Shown in the left frame of Fig. 5 is the time history of the coefficient of interest. The middle and right frames show the radial profiles of the residual stress $\Pi_{r\phi}$, the spectrum averaged parallel wave vector $\langle k_{||}|\delta\phi|^2\rangle$, intensity gradient $d|\delta\phi|^2/dr$ and the zonal flow shear ω_{ZF} during the linear stage ($t = 150$) and nonlinear stage ($t = 350$). The central frame demonstrates the similarity on the shapes of the $\Pi_{r\phi}$, $\langle k_{||}|\delta\phi|^2\rangle$ and $d|\delta\phi|^2/dr$ profiles during the linear stage. During the nonlinear stage, the orientation of the residual stress does not change compared to that in the linear stage, as shown in the right frame. The average correlation coefficients during the nonlinear stage are $C[\Pi^R_{r\phi}, \langle k_{\|}|\delta\phi|^2\rangle] \approx 0.71$ and $C[\Pi^R_{r\phi}, dI/dr] \approx -0.74$, respectively (the sign of correlation indicates the phase relation). This seems to support the generation of residual stress through the intensity-gradient-induced finite $\langle k_{\|}|\delta\phi|^2\rangle$ mechanism. However, it is found that the correlation between intensity gradient and residual stress has the opposite sign at weak $\hat{s}$ compared to that at normal $\hat{s}$, which can not be explained by the traditional intensity gradient mechanism where the sign change of $\hat{s}$ is required for the residual stress orientation change. On the other hand, as zonal flows develop, which can largely affect turbulence transport at saturation [35], zonal flow shear may also contribute to $\Pi^R_{r\phi}$ generation in the nonlinear phase [16]. However, the zonal flow shear correlation with residual stress ($C[\Pi^R_{r\phi}, \omega_{ZF}] \approx -0.5$) is not stronger than that with the intensity gradient. In addition, according to the right frame of Fig. 5, the zonal flow appears not to alter the orientation of the residual stress from linear stage to nonlinear stage. To verify the effect of zonal flow shear, the residual stress profiles with zonal field switched on and off for weak $\hat{s}$ are compared in Fig. 6. The orientation of $\Pi^R_{r\phi}$ profiles for both cases remains changed compared to that for normal $\hat{s}$ case in Fig. 2 A. This demonstrates that the $\Pi^R_{r\phi}$ reversal at weak $\hat{s}$ is not due to zonal flow shear effect. In addition to the effect of the zonal flow, the effect of equilibrium radial electric field E_{r0} induced flow [15, 36] is also examined. In the sensitivity study with respect to E_{r0}, when turning on and off E_{r0}, the observation of $\Pi^R_{r\phi}$ profile reversal from normal to weak $\hat{s}$ remains unchanged. Since E_{r0} is connected to the diamagnetic level velocity via the radial force balance equation, the sensitivity studies indicates that $\Pi^R_{r\phi}$ orientation change in the simulation is not due to the symmetry breaking mechanism related to the diamagnetic level velocity shear [15].

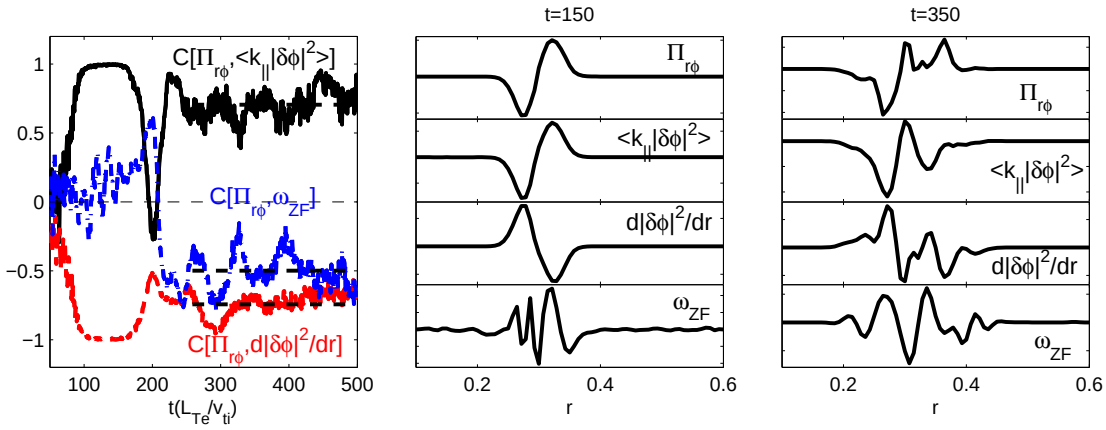

Figure 5. Correlation between residual stress $\Pi^R_{r\phi}$, spectrum weighted parallel wave vector $\langle k_\parallel |\delta\phi|^2\rangle$, turbulence intensity gradient $d|\delta\phi|^2/dr$ and zonal flow shear ω_{ZF}.

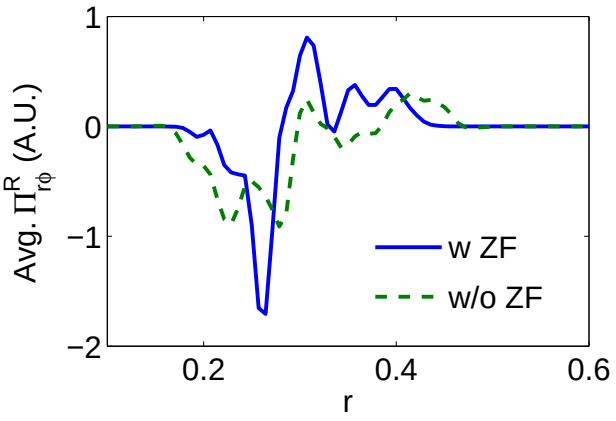

Figure 6. Residual stress with and without zonal flows for $\hat{s}(r_c) \sim 0.1$. Both cases have the opposite orientation of $\Pi^R_{r\phi}$ compared to that for normal $\hat{s}$ case in Fig. 2 A.

4. Interpretation of the intrinsic torque reversal based on mode structure analysis and the complex mixed WKB-full-wave approach

To understand the role of $\hat{s}$ in intrinsic torque reversal, we analyze the radial structure of the poloidal harmonics (radial eigenfunction) $\delta\phi_m(r)$ to demonstrate $\delta\phi_m(r)$'s unusual enhanced radial shift and the consequent $\langle k_\parallel |\delta\phi|^2\rangle$ reversal at low $\hat{s}$. From the correlation analysis, $\langle k_\parallel |\delta\phi|^2\rangle$ appears strongly correlated with the residual stress especially in the linear stage and thus we focus on $\langle k_\parallel |\delta\phi|^2\rangle$. Figure 7 (A and B) shows the radial eigenfunctions from the GTS simulation (the most unstable mode) and the schematics of $\delta\phi_m(r)$ for normal (relatively high) (A, C) and weak $\hat{s}$ (B, D) cases. We use the q profile with on-axis q_{min} in Eq. (3). The parameters are $q(r_c) = 1.5$, $\hat{s}(r_c) = 1.0$, $\kappa_e = 4.5$, $\kappa_i = 1.125$, $\kappa_n = 2.25$ in Fig. 7 A, and $q(r_c) = 1.5$, $\hat{s}(r_c) = 0.2$, $\kappa_e = 6.0$, $\kappa_i = 1.25$, $\kappa_n = 3.0$ in Fig. 7 B. In Fig. 7 A, the poloidal harmonics are localized at the rational mode surface while in Fig. 7 B, the modes with lower amplitude tend to shift away

from the RMS towards the largest amplitude harmonic. The consequence on $\langle k_\parallel |\delta\phi|^2\rangle$ is demonstrated by the schematics in Fig 4 C and D. For simplicity, we choose a single n mode and calculate $\langle k_\parallel |\delta\phi|^2\rangle$ at $r_{n,m}$, the mode rational surface of the harmonic (n,m), where by definition $k_{||}|_{r_{n,m}} = 0$. For normal $\hat{s}$, in the presence of intensity gradient, poloidal harmonics with $m' > m$ (blue line) contribute more to $\langle k_\parallel |\delta\phi|\rangle$ at $r_{n,m}$ than do those with $m' < m$ (red line), and thus $\langle k_\parallel |\delta\phi|^2\rangle = \sum_{m'}(nq - m')|\delta\phi_{m'}|^2/qR < 0$ [19], as shown in Fig. 7 C. However, at weak $\hat{s}$, as shown in Fig. 7 D, the simulations show that the harmonic $m-1$ shifts towards the harmonic (n,m) so strongly that $\langle k_\parallel |\delta\phi|^2\rangle$ is set mainly by modes with lower amplitude, yielding $\langle k_\parallel |\delta\phi|^2\rangle$ reversal as compared to that in Fig. 7 C. It should be noted that in Fig 7 C and D, we intend to identify the mode structure features which lead to the $\langle k_\parallel |\delta\phi|^2\rangle$ reversal at low $\hat{s}$. Meanwhile the overall shift of the radial mode structure found in recent work [6] can also occur but is not likely to be the reason for $\langle k_\parallel |\delta\phi|^2\rangle$ reversal at low $\hat{s}$ in this work as shown in Fig. 7 A and B. In addition, the radial shift of the poloidal harmonics at low $\hat{s}$ in this work is different than that due to equilibrium E_r or zonal E_r shear, as demonstrated by the foregoing correlation and sensitivity studies, and appears to be relevant to the intrinsic torque reversal at weakly positive $\hat{s}$.

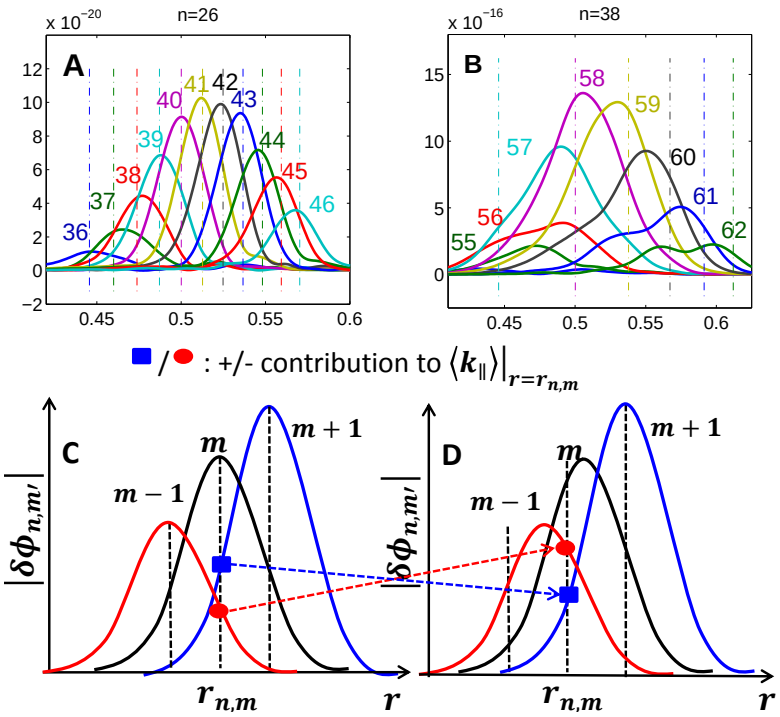

Figure 7. Radial eigenfunction structure for (A) normal and (B) weak $\hat{s}$. For normal $\hat{s}$, $\delta\phi_{m+1}$ contributes more than $\delta\phi_{m-1}$ to $\langle k_\parallel |\delta\phi|^2\rangle$ at r_m (broken line with markers) and thus $\langle k_\parallel |\delta\phi|^2\rangle < 0$. For weak $\hat{s}$, $\delta\phi_{m-1}(r)$ shifts towards the (n,m) mode strongly and sets the sign of $\langle k_\parallel |\delta\phi|^2\rangle$, yielding $\langle k_\parallel |\delta\phi|^2\rangle > 0$.

An analytical interpretation can be obtained from the quasilinear estimate of residual stress and its dependence on $\hat{s}$. The connection between the residual stress

and $\langle k_\parallel |\delta\phi|^2\rangle$ can be seen in the parallel residual stress, which can be estimated as [19]

$$\langle \delta v_r \delta v_\parallel \rangle = -\frac{e}{B_\phi m_i} Re \left\langle \frac{|\gamma_{\mathbf{k}}|}{|\omega_{\mathbf{k}}|^2} \frac{nq}{r} k_\parallel |\delta\phi|^2 \right\rangle \quad . \tag{8}$$

For each n mode $\langle \delta v_r \delta v_\parallel \rangle \propto \langle k_\parallel |\delta\phi|^2\rangle$. A more rigorous derivation relies on the rigorous calculation of the drift wave (ITG/TEM) mode structure based on the gyrokinetic equation in tokamak geometry and the calculation of the parallel, perpendicular and polarization residual stress [5], which will be studied in future work. The purpose of the following analysis is to consider a simple model for both the intensity gradient and the mode structure tilt effects on the reversal of $\langle k_\parallel |\delta\phi|^2\rangle$ on the same footing and to discuss the relevant residual stress orientation change at weakly positive $\hat{s}$. The effect of the $\hat{\theta}_k^R$ has been discussed in [13] in terms of the mode structure tilt. In our work, we also include the intensity gradient effect on the parallel mode structure by introducing the imaginary part $\hat{\theta}_k^I$. We calculate $\langle k_\parallel |\delta\phi|^2\rangle$ by referring to the eigen equation in ballooning representation in the fluid-ion limit with the drive from the non-adiabatic electron taken into account [37, 38, 39], where the parallel mode structure $\delta\hat{\phi}$ is determined by the potential

$$Q = (k_\theta \rho_i)^2 \left[1 + \hat{s}^2 (\hat{\theta} - \hat{\theta}_k)^2\right] - \frac{\omega_D}{\omega} \kappa_c \quad , \tag{9}$$

which consists of the ion finite Larmor radius (FLR) term $(k_\theta \rho_i)^2$ and the ion magnetic drift term $\kappa_c = \cos\hat{\theta} + \hat{s}(\hat{\theta} - \hat{\theta}_k)\sin\hat{\theta}$. Here $\hat{\theta}_k \equiv \hat{\theta}_{k,R} + i\hat{\theta}_{k,I}$ is related to the mode radial envelope A by $A = \exp\{i \int nq' \hat{\theta}_k dr\}$ and the other terms are standard notations in Ref. [37, 38, 39]. It should be noted that historically, $\hat{\theta}_k^I$ has rarely been considered. In our study, $\hat{\theta}_k^I$ is not much smaller than $\hat{\theta}_k^R$ and should be considered. For the TEM simulation in section 2, according to the mode structure in linear simulation, the approximated value with $k_\theta \rho_i \sim 1$, $nq'\hat{\theta}_k^I \sim 10/a$, $\rho/a \sim 1/100$ yields $\hat{s} \times \hat{\theta}_k^I \sim 0.1$ while the tilting angle is $\hat{\theta}_k^R \sim -\pi/10$. To calculate $\hat{s}_{crit}$ and demonstrate the effects of magnetic drift and FLR terms, a parametric scan of $\hat{s}$ is performed based on Eq. (9) by solving the eigenvalue problem for the parallel mode structure. Other parameters correspond to those of GTS simulations. The normalized variable $\langle qR_0 k_{||}\rangle \equiv \sum_m (nq - m)|\delta\phi_m|^2 / \sum_m |\delta\phi_m|^2$ is calculated. As shown in Fig. 8, the black line is the solution with Eq. (9) considered, and as the baseline, it shows that when $\hat{s}$ decreases from normal to weak, $\langle qR_0 k_\parallel\rangle$ crosses $\langle qR_0 k_\parallel\rangle = 0$ at $\hat{s}_{crit} = 0.38$. If we choose $\kappa_c = 0$, $\langle qR_0 k_\parallel\rangle$ always remains positive and close to a saturation value, indicating that the negative value of $\langle qR_0 k_\parallel\rangle$ at weak $\hat{s}$ results from the magnetic drift term. The other curves have FLR or κ_c terms artificially suppressed or amplified. They show that increasing κ_c and decreasing ion FLR effect have a similar impact on increasing $\hat{s}_{crit}$ as compared to the baseline. The competition between FLR and κ_c terms determines the value of $\hat{s}_{crit}$, at which $\langle qRk_\parallel\rangle = 0$. This competition is reminiscent of transition between the toroidal branch and the slab branch of the drift wave, depending on $\hat{s}$ [37]. However, previous work focused on the eigenfrequency and not on the asymmetry of the parallel mode structure. The novelty of the analysis in this work is the consideration of the synergy of the toroidal coupling and intensity gradient effects. On one hand, the magnetic drift term

$\kappa_c = \cos\hat{\theta} + \hat{s}(\hat{\theta} - \hat{\theta}_k)\sin\hat{\theta}$ introduces toroidal coupling which brings in modulations on the otherwise anti-well potential Q [37]. On the other hand, the radial intensity gradient in $\hat{\theta}_k$ introduces symmetry breaking in κ_c. The synergy of these two effects leads to the radial eigenfunction shift and reversal of $\langle qR_0k_{||}\rangle$ at weak $\hat{s}$. This symmetry breaking mechanism is different than those due to intensity gradient [19] or $\mathbf{E}\times\mathbf{B}$ shear [16, 36, 40].

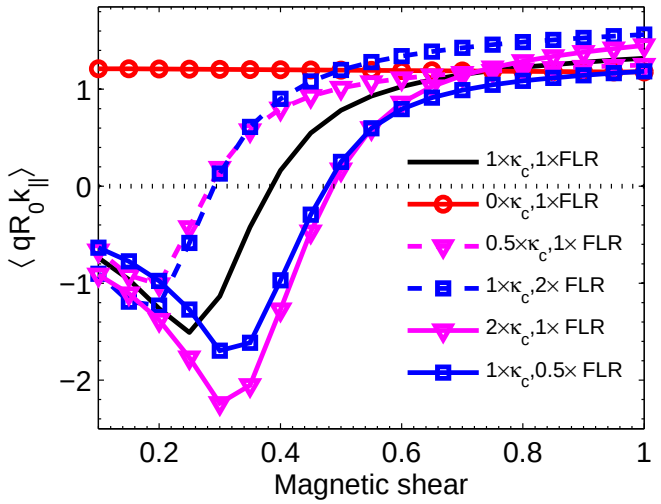

Figure 8. $\langle qR_0k_{||}\rangle$ with different amplification factors of magnetic drift (κ_c) and ion FLR effect. The black line is $\langle qR_0k_{||}\rangle$ obtained from Eq. (9) for TEM branch while the other lines are that with different amplification factors of FLR or κ_c terms. Parameters are $\hat{\theta}_k^R = -\pi/10$, $\hat{s}\times\hat{\theta}_k^I = 0.1$.

The effect of the tilting angle and the intensity gradient is studied in the parametric scans with respect to $\hat{\theta}_k^R$ and $\hat{\theta}_k^I$ for different values of $\hat{s}$. The value of $\hat{\theta}_k^R$ is set to zero in the $\hat{\theta}_k^I$ scan and vice versa. Figure 9 shows that the magnitude of $\langle qR_0k_{||}\rangle$ increases when the tilting angle $\hat{\theta}_k^R$ or the intensity gradient variable $\hat{\theta}_k^I$ increases. However, as shown in Fig. 9 B, the $\hat{s}$ value affects the sign of $\langle qR_0k_{||}\rangle$ and the parallel residual stress. The trend of $\langle qR_0k_{||}\rangle$ with respect to the intensity gradient and $\hat{s}$ is consistent with the results of the GTS simulation in Fig. 3 and the observed correlation between the intensity gradient and residual stress in Fig. 5 although the model in this section is greatly reduced. It should be noted that in principle, the dominance of either the tilting angle or the intensity gradient may depend on the parameters, e.g., the first and second derivatives of temperature and density. Recent work reports the possible dominance of the tilting angle effect in the ITG study with broader gradient profile (corresponding to $r_w \approx 0.325$ in Eq. (4)) and $\hat{s}(r_c) = 0.78$ [20]. In our work, based on the foregoing analyses in a broader $\hat{s}$ regime with gradient width relevant to LHCD experiment, the intensity gradient mechanism appears to be important and the value of $\hat{s}$ is crucial for the sign of the residual stress.

The poloidal harmonic $\delta\phi_m(r)$'s radial shift can be obtained as $\Delta r_m = (-1/nq')(2|\sigma|^2\hat{\theta}_{k,I}/\sigma_R - qR_0\langle k_{||}\rangle)$, based on the transform formula between

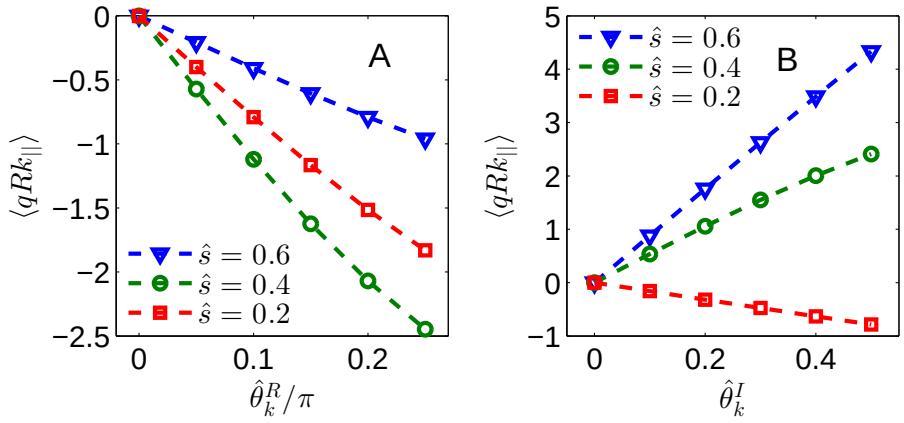

Figure 9. The effect of the global mode structure tilting angle $\hat{\theta}_k^R$ for $\hat{\theta}_k^I = 0$ (A) and the effect of the intensity gradient variable $\hat{\theta}_k^I$ for $\hat{\theta}_k^R = 0$ (B) on $\langle qR_0k_{\|}\rangle$ for various magnetic shear values.

the parallel mode structure and the poloidal harmonics [22], where $\sigma = -i(\omega_{ti}/\omega)\sqrt{b - [(\hat{s} - 1/2)C + i\hat{s}\hat{\theta}_{k,I}S/2]\omega_D/\omega}$, $b = (k_\theta\rho_i\hat{s})^2$, $S = \sin\hat{\theta}_{k,R}$, $C = \cos\hat{\theta}_{k,R}$. In Eq. (9), at normal to large $\hat{s}$, FLR effects ($\propto \hat{s}^2$) dominate over the magnetic drift term ($\propto \hat{s}$). An analytical solution can be obtained as $\langle k_{\|}\rangle|_{\hat{s}\to\infty} = (2/qR_0)(|\sigma|^2\hat{\theta}_{k,I}/\sigma_R)$ and $\Delta r_m|_{\hat{s}\to\infty} = 0$. Thus $\delta\phi_m(r)$ peaks at its rational mode surface as $\hat{s} \to \infty$. When $\hat{s}$ decreases, the magnetic drift effects become important, inducing significant radial shift, which causes $\langle k_{||}\rangle$ reversal. The solution of eigenvalue problem in high and low $\hat{s}$ correspond to the slab and toroidal branches respectively [37] while the eigenfunction analyses give zero and significant radial eigenfunction shift and thus $\langle k_{\|}\rangle$ reversal between them. It should be noted that the eigen equation here does not include zonal flow or equilibrium flow, thus the radial shift in the low $\hat{s}$ regime discussed here is indeed a different mechanism for $k_{||}$ symmetry breaking, distinct from previous results which relied on the $\mathbf{E}\times\mathbf{B}$ shear symmetry breaking mechanism [15, 16, 36, 40].

5. Relevance to intrinsic torque reversal experiments with LHCD on Alcator C-Mod

Our finding of critical magnetic shear for intrinsic torque reversal gives an interpretation of the the Alcator C-Mod experimental results. We refer to three Alcator C-Mod LHCD discharges with plasma current 0.32 MA, 0.59 MA and 0.91 MA. The profiles of the ion temperature, electron temperature, electron density and the corresponding normalized radial gradient are shown in Fig. 10, which suggests that the 0.91 MA discharge is TEM favorable due to the increased electron temperature and the consequent decreased electron collision. More details of the Alcator C-Mod rotation experiments with LHCD can be found in [41]. According to our linear simulation, the 0.32 MA discharge is ITG dominant due to the large ion temperature gradient for $r < 0.6$ while the other two are TEM dominant. As a result, we focus on the 0.59 MA and 0.91 MA cases (with

$\hat{s}(r = 0.3) = 0.2$ and 0.5 respectively) in order to verify the effect of magnetic shear without ITG-TEM transition.

First we identify the critical magnetic shear $\hat{s}_{crit}$ for the C-Mod parameters by parametric studies with respect to $\hat{s}(r = 0.5)$. The 0.91 MA discharge is defined as the LHCD base case, which is characterized by $q = 1.38$, $R_0/L_{Ti} = 4.29$, $R_0/L_{Te} = 10.75$ and $R_0/L_{ne} = 3.38$ at $r = 0.5$, $\theta = 0$. The created fitted normalized gradient profile (blue solid line) of the LHCD base case is shown in Fig. 11. The average second derivative $\partial(R_0/L_X)/\partial r$ for $0.35 < r < 0.5$ is fitted to the experimental one by matching the R_0/L_X value to that of the original experimental value at $r = 0.35$ and $r = 0.5$. The q profiles for parametric scan are generated using Eq. (3), with $q(r = 0.5) = 1.38$ and specific $\hat{s}(r = 0.5)$. With the corresponding generated equilibria, we can calculate the normalized residual stress and identify the value of $\hat{s}_{crit}$ relevant to the C-Mod LHCD discharges. Shown in Table 3 are the characteristic values at $r = 0.5$ for experimental LHCD base case (0.91 MA) and for parametric scans with respect to $\hat{s}$ in ITG and TEM studies in this section. The radial structure of the normalized residual stress from GTS simulations in Fig. 12 suggests $\hat{s}_{crit}^{TEM} \approx 0.4$ for TEM and $\hat{s}_{crit}^{ITG} = 0.92 \pm 0.2$ for ITG mode with the chosen parameters in Table 3.

Table 3. The characteristic values at $r = 0.5$, $\theta = 0$ for experimental LHCD base case and for parametric scans with respect to $\hat{s}$. The TEM case is closer to the experimental (Exp.) case while the ITG case is constructed by exchanging the ion and electron temperature parameters.

	R_0/L_{Ti}	R_0/L_{Te}	R_0/L_{ne}	$T_i(keV)$	$T_e(keV)$	$n_e(10^{13}/cm^3)$	$\hat{s}$
Exp.	4.29	10.75	3.38	0.72	1.38	7.73	0.72
TEM	1.69	10.75	3.38	0.72	1.38	7.73	0.20, 0.40, 0.72
ITG	10.75	1.69	3.38	1.38	0.72	7.73	0.32, 0.72, 1.12

The simulation based on the experimental profiles is performed for more realistic comparison with the experimental observations. In the nonlinear simulation, the simulation domain covers $0.05 < r < 0.80$ and the normalized gradient is modified outside $r = 0.725$ as shown in Fig. 11 (red dashed line), since we focus on the physics in the core, and since the experimentally observed toroidal rotation change occurs for $r < 0.5$ [9]. Compared to the linear results, the residual stress spreads towards the magnetic axis side as shown in Fig. 13 A. This suggests that the large electron temperature gradient near $r = 0.5$ can have an impact on the toroidal rotation change in the inner region ($r < 0.5$). In Fig. 13 B, the normalized residual stress $\hat{\Pi}_{r\phi}$ for the 0.91 MA discharge is positive for $r < 0.5$, which leads to the counter-current toroidal velocity increment, while for the 0.59 MA discharge, $\hat{\Pi}_{r\phi}$ has a lower magnitude for $r < 0.5$. In addition, $\hat{\Pi}_{r\phi}$ decreases to negative for $r < 0.35$ for the 0.59 MA discharge, where the local magnetic shear $\hat{s}(r = 0.35) = 0.34$, which suggests that the sign of $\hat{\Pi}_{r\phi}$ is related to $\hat{s}_{crit}^{TEM} \approx 0.4$ shown in Fig. 12 B. Considering that the experimentally observed toroidal velocity change before and after LHCD is $\Delta V_\phi \approx 5$ km/s for the 0.59 MA discharge and $\Delta V_\phi \approx -30$ km/s for the 0.91 MA discharge, the magnitude of $\hat{\Pi}_{r\phi}$

shown in Fig. 13 B also reflects the experimental trend. However, the calculation of the rotation profile, in principle, relies on transport time scale simulation, requiring the consideration of other effects such as momentum pinch [12, 42] and the coupling between the edge plasma and the wall, which is beyond the scope of this work.

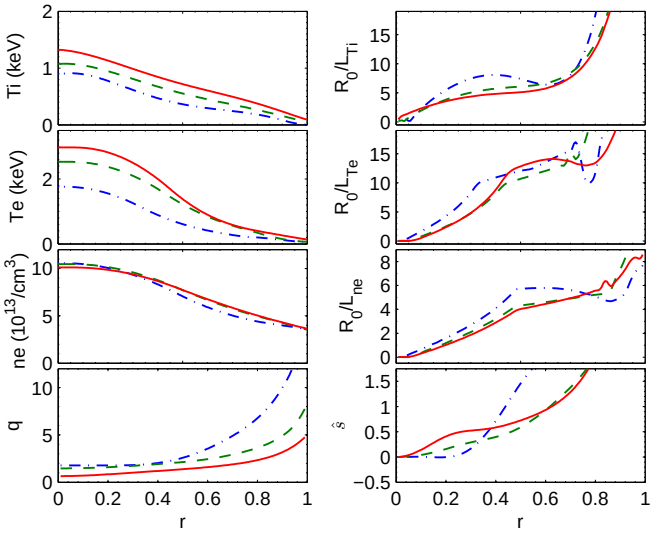

Figure 10. The profiles of Alcator C-Mod LHCD discharges with plasma current 0.32 MA (blue dotted dash-dot line), 0.59 MA (green dashed line) and 0.91 MA (red solid line). The shot numbers are 1110128015, 1110128017 and 1110128020 respectively.

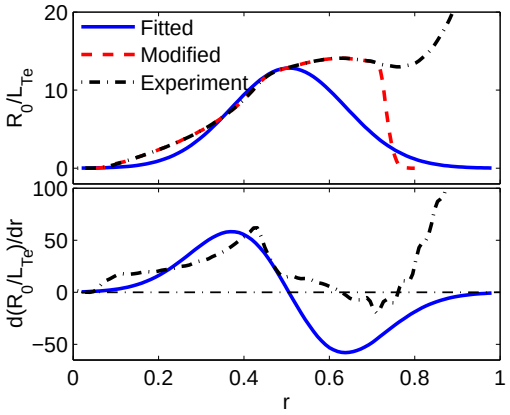

Figure 11. The original experimental profile (black dash-dot line), the modified profile for nonlinear simulation (red dashed line) and the created fitted profiles for the linear parametric scan with respect to $\hat{s}(r = r_c)$ (blue solid line) of the LHCD base case. The upper and lower frames are the profiles of $R_0/L_{Te} \equiv R_0|\nabla r|\partial \ln T_e/\partial r$ and the derivative of R_0/L_{Te} at $\theta = 0$, respectively.

6. Summary and conclusions

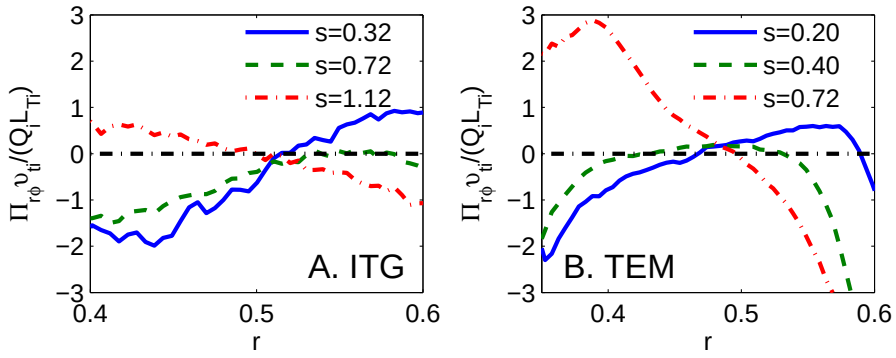

Figure 12. The radial structure of the normalized residual stress for ITG mode (left) and TEM (right) in various magnetic shear $\hat{s}(r = r_c)$, which suggests that $\hat{s}_{crit}^{ITG} = 0.92 \pm 0.2$ and $\hat{s}_{crit}^{TEM} \approx 0.4$ for the parameters in Table 3.

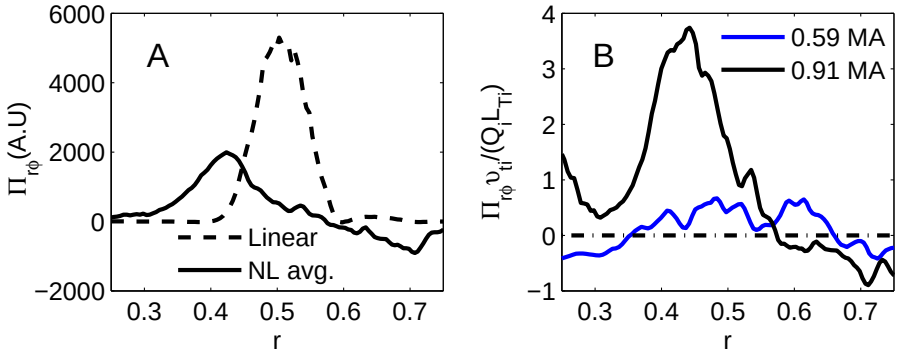

Figure 13. A. The residual stress profile of linear (dashed line) and nonlinear stage for the LHCD base case. B. The normalized residual stress profile for the 0.59 MA and 0.91 MA LHCD discharges (average value during nonlinear stage). The profile in $r < 0.25$ are not displayed due to the small magnitude of the turbulence intensity and the residual stress therein.

The main results of this work are as follows:

- Intrinsic torque τ_I reverses from the co-current direction to the counter-current direction when the magnetic shear is lower than a finite positive value $\hat{s}_{crit}$. For model equilibria and specific profiles, the predicted critical magnetic shear is $\hat{s}_{crit}^{ITG} \approx 1.1$ for ITG mode and $\hat{s}_{crit}^{TEM} \approx 0.3$ for TEM.
- Strong correlation between the turbulence intensity and the residual stress has been demonstrated, which supports the residual stress generation mechanism due to the turbulence intensity. Sensitivity studies demonstrate that zonal flow shear and mean flow shear do not change the phenomenon of the intrinsic torque reversal.
- Analysis identifies that the τ_I reversal is related to an important feature of symmetry breaking mechanism, namely, the radial eigenfunction shift due to the synergy of toroidal coupling and intensity gradient. This mechanism is particular to toroidal geometry and is not the continuation of the traditional intensity gradient

symmetry breaking mechanism to weak $\hat{s}$ [19]. The reversal is not merely due to the global mode tilt due to profile shearing either, where intensity gradient mechanism is thought to be unimportant [13].

- The parametric scan identifies the critical magnetic shear for intrinsic torque reversal with fitted profiles relevant to Alcator C-Mod LHCD rotation experiments, i.e., $\hat{s}_{crit}^{ITG} \approx 0.92$ and $s_{crit}^{TEM} \approx 0.4$. The nonlinear simulation results with realistic profiles are consistent with the experimental observations in terms of torque direction and critical magnetic shear $\hat{s}_{crit}$ for torque reversal.

Our finding of the intrinsic torque reversal at a finite positive value of the magnetic shear could be important for interpreting experimental results on different tokamak devices. The rotation reversal of Ohmic discharges has been observed on various tokamak devices, such as TCV [43], ASDEX Upgrade [44] and C-Mod [7], where the critical density has been thought to be more relevant, while the effects of magnetic shear have been essentially ignored until the recent LHCD rotation experiments [9]. According to our results, the database of the rotation experiments might be better classified and the intrinsic torque direction might be better predicted according to multiple parametric variables including the magnetic shear, mode type and collisionality. Another significant aspect of our work is its relevance to ITB formation. According to the Optimal Shear (OS) experiments on JET, the toroidal flow shear and $\hat{s}$ are crucial factors for ITB formation. Therefore, understanding the effect of the residual stress on rotation profile formation at weak magnetic shear is important for the study of the ITB formation, especially for large-size devices such as ITER or DEMO, where NBI is not sufficient to drive the toroidal rotation. In this work, we focused on the residual stress induced by the radial variation. It might be important to consider turbulent acceleration [17, 18], polarization drift [45], turbulence spreading [46], neoclassical effects [30, 31] and their behavior at weak magnetic shear. The contribution from different mechanisms on the rotation profile formation will be studied in our future work.

Acknowledgments

This work is supported by CER, DOE Grant for CMTFO DE-FG02-OER54871, and U.S. DOE-PPPL Contract DE-AC02- 09CH11466. The support from L. Zakharov on equilibrium reconstruction is acknowledged. Simulations were performed at the National Energy Research Scientific Computing Center (NERSC). Z.L. appreciates the discussion with F. Zonca and J. Lang.

[1] Rüdiger G 1989 *Differential Rotation and Stellar Convection: Sun and Solar-Type Stars* (Gordon and Breach, New York)
[2] Hughes D W, Rosner R and Weiss N 2007 *The Solar Tachocline* (Cambridge University Press, Cambridge)
[3] Baldwin M P, Rhines P B, Huang H P and McIntyre M E 2007 *Science* **315** 467
[4] Rice J E *et al.* 2004 *Phys. Plasmas* **11** 2427
[5] Diamond P H *et al.* 2013 *Nucl. Fusion* **53** 104019

[6] Bondeson A and Ward D J 1994 *Phys. Rev. Lett.* **72** 2709
[7] Rice J E *et al.* 2011 *Phys. Rev. Lett.* **107** 265001
[8] Shi Y J *et al.* 2011 *Phys. Rev. Lett.* **106** 235001
[9] Rice J E *et al.* 2013 *Phys. Rev. Lett.* **111** 125003
[10] Ida K, Miura Y, Matsuda T, Itoh K, Hidekuma S, Itoh S I and JFT-2MGroup 1995 *Phys. Rev. Lett.* **74** 1990
[11] Challis C D *et al.* 2001 *Plasma Phys. Control. Fusion* **43** 861
[12] Peeters A, Angioni C *et al.* 2011 *Nucl. Fusion* **51** 094027
[13] Camenen Y, Idomura Y, Jolliet S and Peeters A G 2011 *Nucl. Fusion* **51** 073039
[14] Camenen Y, Peeters A G, Angioni C, Casson F J, Hornsby W A, Snodin A P and Strintzi D 2009 *Phys. Plasmas* **16** 062501
[15] Waltz R, Staebler G and Solomon W 2011 *Phys. Plasmas* **18** 042504
[16] Wang W X, Hahm T S, Ethier S, Rewoldt G, Lee W W, Tang W M, Kaye S M and Diamond P H 2009 *Phys. Rev. Lett.* **102** 035005
[17] Wang L and Diamond P H 2013 *Phys. Rev. Lett.* **110** 265006
[18] Garbet X, Esteve D, Sarazin Y, Abiteboul J, Bourdelle C, Dif-Pradalier G, Ghendrih P, Grandgirard V, Latu G and Smolyakov A 2013 *Phys. Plasmas* **20** 072502
[19] Gürcan Ö D, Diamond P H, Hennequin P, McDevitt C J, Garbet X and Bourdelle C 2010 *Phys. Plasmas* **17** 112309
[20] Buchholz R, Camenen Y, Casson F, Grosshauser S, Hornsby W, Migliano P and Peeters A 2014 *Phys.Plasmas* **21** 062304
[21] Kwon J M, Yi S, Rhee T, Diamond P H, Miki K, Hahm T S, Kim J Y, Gürcan Ö D and McDevitt C J 2012 *Nucl. Fusion* **52** 013004
[22] Lu Z X, Zonca F and Cardinali A 2012 *Phys. Plasmas* **19** 042104
[23] Wang W X, Diamond P H, Hahm T S, Ethier S, Rewoldt G and Tang W M 2010 *Phys. Plasmas* **17** 072511
[24] Wang W X, Hahm T S, Ethier S, Zakharov L E and Diamond P H 2011 *Phys. Rev. Lett.* **106** 085001
[25] Zakharov L E and Pletzer A 1999 *Phys. Plasmas* **6** 4693
[26] Wang W X, Nakajima N, Okamoto M and Murakami S 1999 *Plasma Phys. Control. Fusion* **41** 1091
[27] Hinton F and Hazeltine R 1976 *Rev. Mod. Phys.* **48** 239
[28] Wang W X, Tang W M, Hinton F L, Zakharov L E, White R B and Manickam J 2004 *Comput. Phys. Commun.* **164** 178
[29] Wang W X, Lin Z, Tang W M, Lee W W, Ethier S, Lewandowski J L V, Rewoldt G, Hahm T S and Manickam J 2006 *Phys. Plasmas* **13** 092505
[30] Parra F I and Catto P J *Plasma Phys. Control. Fusion* **52** 045004
[31] Barnes M, Parra F I, Lee J P, Belli E A, Nave M F F and White A E 2013 *Phys. Rev. Lett.* **111** 055005
[32] Idomura Y 2014 *Phys. Plasmas* **21** 022517
[33] Waltz R E, Kerbel G D and Milovich J 1994 *Phys. Plasmas* **1** 2229
[34] Wang W X, Hahm T S, Lee W W, Rewoldt G, Manickam J and Tang W M 2007 *Phys. Plasmas* **14** 072306
[35] Watanabe T H, Sugama H and Ferrando-Margalet S 2008 *Phys. Rev. Lett.* **100** 195002
[36] Gürcan Ö D, Diamond P H, Hahm T S and Singh R 2007 *Phys. Plasmas* **14** 042306
[37] Chen L and Cheng C Z 1980 *Phys. Fluids* **23** 2242
[38] Tang W M 1978 *Nucl. Fusion* **18** 1089
[39] Romanelli F and Zonca F 1993 *Phys. Fluids B* **5** 4081
[40] Dominguez R R and Staebler G M 1993 *Phys. Fluids B* **5** 3876
[41] Rice J *et al.* 2013 *Nucl. Fusion* **53** 093015
[42] Hahm T S, Diamond P H, Gurcan O D and Rewoldt G 2007 *Phys. Plasmas* **14** 072302

[43] Duval B, Bortolon A, Karpushov A, Pitts R, Pochelon A, Scarabosio A and Team T 2007 *Plasma Phys. Control. Fusion* **49** B195
[44] Angioni C *et al.* 2011 *Phys. Rev. Lett.* **107** 215003
[45] McDevitt C J, Diamond P H, Gürcan O D and Hahm T S 2009 *Phys. Rev. Lett.* **103**(20) 205003
[46] Naulin V, Juul Rasmussen J, Dam M and Brøns M 2014 *41st EPS Conference on Plasma Physics, Berlin*